Burning characteristics of aluminum-air flames

R. Lomba , F. Lespinasse[1,2], V. Lago[1], C. Chauveau[1], and F. Halter[1,2]

[1]CNRS, 1C Avenue de la Recherche Scientifique, Orléans Cedex 2, France
[2]Université d'Orléans, 8 rue Léonard de Vinci, Orléans Cedex 2, France

1 Introduction

Metal particles present an interesting potential as a carbon-free energy carrier. Indeed, they are highly energetic, and its combustion in atmospheric air could provide the specific energy and power density that metal-air batteries are still struggling to achieve. In order to better evaluate this potential, it is necessary to know the metal-air aerosol laminar burning velocity, which is a fundamental property describing the mixture's reactivity, heat production, and heat transfer. However, experimental data on the burning velocity of metal-air aerosols are still scarce and scattered. Moreover, metal flames are subjected to a series of particular effects such as the presence of a particle size distribution, implying different burning rates for particles of different sizes in the powder, and possibly scale-dependent influence of radiation [1]. These effects raise even the question of whether a non-stretched laminar burning velocity can be properly defined for metal dust clouds [2]. Therefore, in order to reduce such uncertainties on the burning velocity measurements, it is necessary to work under well-controlled conditions.

Among the different possible metal choices for an energy carrier, this work focuses on aluminum, since it presents satisfying energy density and specific energy. Furthermore, the development of a laminar dust burner inspired by previous works in the literature [3, 4] is presented. The experimental setup is capable of stabilizing aluminum-air flames through the generation of well-controlled dust aerosols. Various optical diagnostics, such as high-speed tomography, direct visualization of AlO(g) emissions and spectroscopy, were conducted in order to measure the flame properties. The results are then compared with the existing literature, and analyzed in a context of zero-carbon power generation.

2 Experimental Setup

The aluminum powder used in this work is pure (> 99.8 %) and spherical, with a Sauter mean diameter of 7.1 μm and a narrow size distribution. The powder characteristics are further described in a previous work [5]. A schematic of the experimental apparatus used is shown in figure 1. It consists of a stirred powder reservoir, which is placed over a scale and connected to one end of an ejector nozzle. An air flow is supplied to the other end of the ejector nozzle, creating a depressurization inside thereof. This depressurization

Correspondence to: fabien.halter@cnrs-orleans.fr

generates a suction flow of aluminum particles and atmospheric air, and disperses the powder into the main body of the burner, forming a turbulent flow. This flow is then laminarized and finally contracted at the exit. The contraction profile is such that boundary layer is crushed and a flat velocity profile is obtained at the burner exit. Around the burner rim, an annular methane-air pilot flame of 1.5 mm of thickness is stabilized in order to improve the flame stabilization. Ignition is then achieved by supplying a methane flow rate to the main flow of the burner, which is ignited by the annular pilot flame, creating a hybrid Al/CH_4-air flame structure. Once the hybrid flame is stable, the methane flow rate is removed, thus allowing an aluminum-air flame to stabilize itself at the burner exit. The flame is then characterized using a spectrometer, a tomography setup, and a camera and filter set in order to visualize the flame emissions.

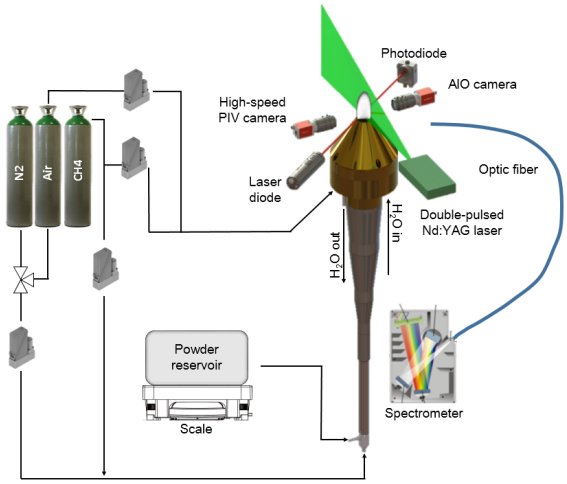

Figure 1: Schematic of the experimental setup.

The aerosol flow at the burner exit is characterized by a particle image velocimetry (PIV) setup, using the aluminum particles themselves as trackers. Under the operating conditions, the Stoke's number associated with the particles is $Stk \approx 10^{-3} \ll 1$, implying that the aluminum particles closely follow the air streamlines and are stationary with respect to the gaseous phase. An example of a PIV image, along with the mean velocity profile extracted exactly at the burner exit, is shown in figure 2. The profile is flat and symmetric, and the total gaseous flow rate is obtained by integrating the mean velocity profile. Figure 2 also shows a good qualitative spatial homogeneity of the dust concentration afar from the boundary layers.

The total air flow rate Q_T is calibrated as a function of the powder mass flow rate $\dot{m}$, thus allowing the definition of a nominal dust concentration at the burner entrance, $\frac{\dot{m}}{Q_T}$. The powder mass flow rate is obtained through the scale measurements of the dust reservoir mass, as illustrated in figure 3, in which m_T is the total mass of powder dispersed in a given run. However, in order to obtain the dust concentration at the burner exit B, it is still necessary to take into account the powder accumulation at the walls inside the experimental device. For such, two distinct methods were used. The first one consists of comparing the weighing measurements described above with the mass difference of the burner itself before and after a run, dM: $B = \left(1 - \frac{dM}{m_T}\right) \frac{\dot{m}}{Q_T}$. The second method consists of studying the attenuation of a laser beam crossing the dust flow (figure 1) with Beer-Lambert's law and the refractive indexes given in [6] in order to obtain the instantaneous dust concentration. The laser attenuation measurements show that the concentration is temporally stable. A calibration campaign comprised of several measurement points with distinct mass flow rates and run duration, is undertaken, and the resulting calibration law is shown on the right in figure

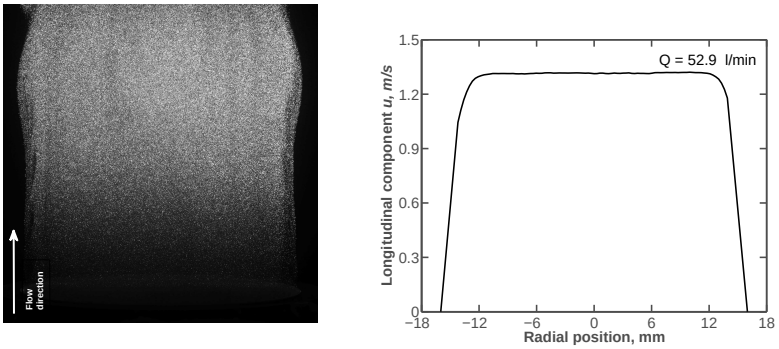

Figure 2: Left: example of PIV image of the non-reactive aerosol flow; right: mean velocity profile extracted exactly at the burner exit.

3. These results show that the weighing and laser attenuation measurements are in good agreement, and that the obtained calibration law is able to determine the dust concentration within 8% of the aluminum-air equivalence ratio with a confidence level of 95%.

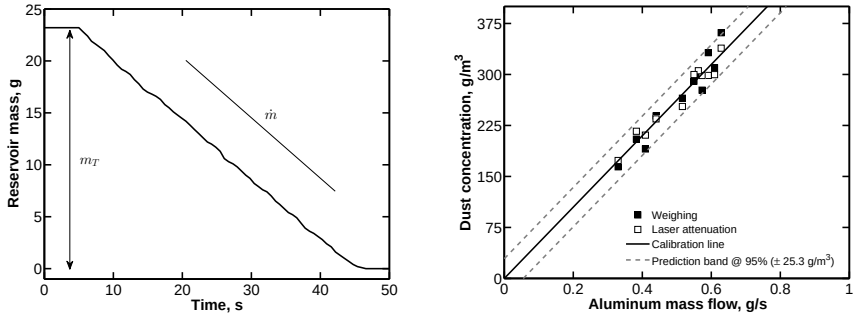

Figure 3: Left: temporal evolution of the dust reservoir mass; right: Dust concentration calibration law.

3 Results

Once stabilized at the burner exit, the metal dust flame produces a very intense light that can be analyzed through emission spectroscopy. Indeed, this light signal emitted by the combustion of the metal particles is composed of two distinct contributions. A first part is due to the thermal excitation of the condensed combustion products, and corresponds to a continuous emission background. It was observed that this emission background can be well-represented by a straight line between 400 nm and 600 nm. Therefore, a fitting algorithm is adjusted to the condensed phase emissions and thereafter subtracted from the flame spectrum. The resulting spectrum after this subtraction corresponds to the emission lines originating from the gaseous species. The main features of the gaseous part of the aluminum flame spectrum are the aluminum vapor lines at 394.3 nm and 396 nm, and the $B^2\Sigma^+ - X^2\Sigma^+$ (blue-green) band system of gaseous aluminum monoxide.

It is possible to determine the temperature which better describes the observed AlO emissions. By assuming a thermal equilibrium between all the species in the reaction zone, the calculated AlO temperature can be

associated to the flame temperature. The fitting process used to determine this flame temperature is described by [7], and consists of a line-by-line simulation of the AlO spectrum based on the spectroscopic constants and relative band strengths from [8, 9]. Figure 4 (left) illustrates an example of an emission spectrum fitting result, obtained for an aluminum-air equivalence ratio of ϕ = 1.3. The emission line at 519.3 nm observed experimentally is not described in the fitting algorithm, and therefore is not taken into account for temperature calculation. Figure 4 (right) shows the results obtained as a function of the dust concentration of the aerosol. Each point in this figure corresponds to an average of 100 spectra. The flame temperature is observed to be constant for all the dust concentrations studied, and is about 3146 K $\pm$ 180 K. This value is 400 K below the adiabatic flame temperature, and is in good agreement with the temperature measurements of the condensed phase carried out in previous experiments in a constant volume chamber [5].

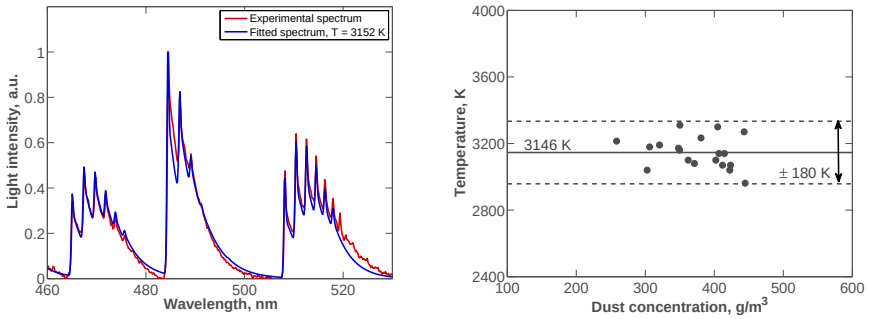

Figure 4: Left: Simulated spectrum superposed to the experimental AlO; right: Aluminum-air flame temperatures as a function of the aluminum dust concentration.

The burning velocity S_L is defined as the rate at which fresh gases move through the combustion wave in the direction normal to the wave surface [10]. In the dust burner setup, the mass conservation principle yields the relationship $S_L = \frac{Q_T}{A}$, where Q_T is the total airflow at the burner exit, and A is the surface area of the flame. The latter can be obtained by the numerical integration of the rotational figure formed by the flame contour. Therefore, the burning velocity can be obtained through the flame contour detection. For such, the flame was observed through two distinct methods: laser sheet tomography and direct visualization of the AlO(g) emissions, as illustrated in figure 5.

In the tomography images, which constitute an instantaneous planar visualization of the Mie-scattering, three different regions can be observed: a fresh mixture region, where the scattering is identical to the cold-flow PIV images (figure 2); a dark region; and a burned mixture region. The study of the velocity field of the reacting flow show that the aerosol strain rate is weak ($< 100\ \mathrm{s}^{-1}$), and that its velocity reaches its minimum at the frontier between the fresh mixture and the dark zone. The frontier between the burned mixture region and the dark zone is where the flame emission at 532 nm is most intense, which can be attributed to the region where most of the alumina condensation occurs. Therefore, the absence of Mie-scattering in the dark region can be explained by a drop in particle density in the preheat zone of the flame followed by aluminum evaporation. The frontier between this zone and the fresh mixture was therefore taken as the flame front position.

In order to validate the burning velocity measurements obtained through laser sheet tomography, direct visualizations of the AlO emissions were also conducted. Indeed, aluminum monoxide is a well-known combustion intermediate, and is often used as an indicator of the flame front position [11]. For both methods, the burning velocities obtained were observed to be roughly constant for dust concentrations between $0.8 <$

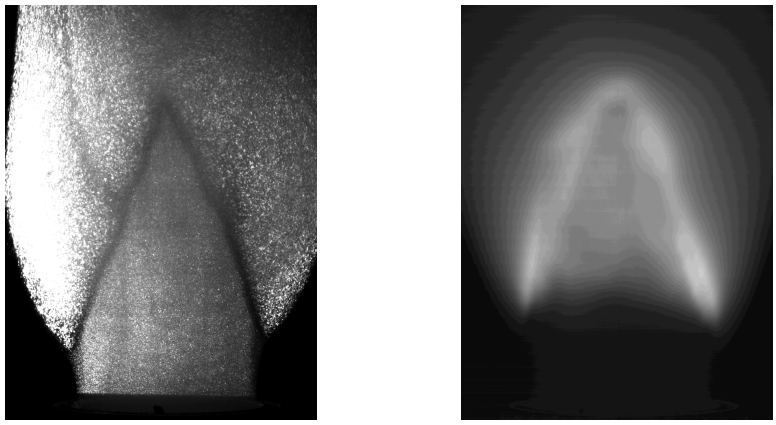

Figure 5: Left: tomography image of an aluminum-air flame; right: mean image of the AlO emissions of an aluminum-air flame.

$\phi < 1.5$, with mean values of 28.5 cm/s when using tomography and 32 cm/s when using AlO visualization. Although a good agreement is obtained, the AlO method integrates temporal instabilities of the flame front position and artificially thickens the flame, causing an overestimation of the burning velocity. For this reason, tomography is considered a more reliable method.

Figure 6 shows the burning velocity results obtained with flame tomography and compares them with existing literature for aluminum powder at about the same mean diameter. The stability of the burning velocity regarding the equivalence ratio was previously observed in [4]. The authors attributed this behavior to the large density difference between air and aluminum particles. Indeed, the addition of aluminum to the aerosol doesn't dilute the oxygen concentration, and the burning rate at each individual particle remains roughly constant. It can also be observed in figure 6 that the results obtained in this work present a lower reproducibility error when compared to previous works, highlighting the importance of working under well-controlled conditions and the choice of the optical diagnostic.

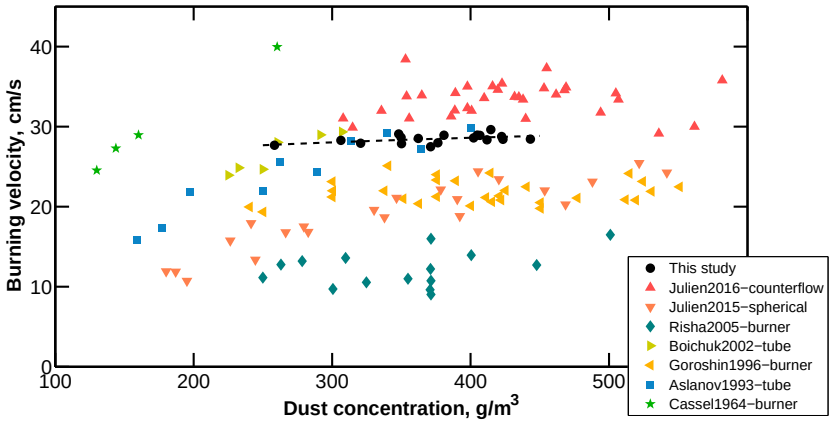

Figure 6: Burning velocities for aluminum-air flames at different dust concentrations.

4 Conclusions

The dust burner presented in this work is capable of generating a dust aerosol with homogeneous dust concentration and a flat velocity profile. As a result, the experimental setup is capable of stabilizing aluminum-air flames at low strain rates and extracting reliable burning velocity measurements through the use of instantaneous flames contour detection using high-speed tomography. Regarding the use of aluminum-air combustion for power generation, it is interesting to note that the burner device has an estimated power output of about 8 kW. Indeed, at a mean powder diameter of 7 μm, the results presented show that aluminum should be as reactive as classical hydrocarbon fuels, presenting similar specific energies and similar burning velocities. Therefore, metals, and in particular aluminum, can be considered as a potential candidate for a clean, renewable and dense energy carrier.

References

[1] P. Julien, J. Vickery, S. Goroshin, D. L. Frost, and J. M. Bergthorson, "Freely-propagating flames in aluminum dust clouds," *Combustion and Flame*, Aug. 2015.

[2] P. Julien, S. Whiteley, M. Soo, S. Goroshin, D. L. Frost, and J. M. Bergthorson, "Flame speed measurements in aluminum suspensions using a counterflow burner," *Proceedings of the Combustion Institute*, 2016.

[3] S. Goroshin, M. Bidabadi, and J. Lee, "Quenching distance of laminar flame in aluminum dust clouds," *Combustion and Flame*, vol. 2180, pp. 147–160, 1996.

[4] S. Goroshin, I. Fomenko, and J. Lee, "Burning velocities in fuel-rich aluminum dust clouds," *Symposium (International) on Combustion*, vol. 26, no. 2, pp. 1961–1967, Jan. 1996.

[5] R. Lomba, S. Bernard, P. Gillard, C. Mounam-Rousselle, F. Halter, C. Chauveau, T. Tahtouh, and O. Guzet, "Comparison of combustion characteristics of magnesium and aluminum powders," *Combustion Science and Technology*, vol. 188, no. 11, pp. 1–21, 2016.

[6] A. D. Rakic, A. B. Djurišic, J. M. Elazar, and M. L. Majewski, "Optical Properties of Metallic Films for Vertical-Cavity Optoelectronic Devices," *Applied Optics*, vol. 37, no. 22, p. 5271, 1998.

[7] J. Arnold, E. Whiting, and G. Lyle, "Line by line calculation of spectra from diatomic molecules and atoms assuming a voigt line profile," *Journal of Quantitative Spectroscopy and Radiative Transfer*, vol. 9, no. 6, pp. 775–798, Jun. 1969.

[8] H. Partridge, S. R. Langhoff, B. Lengsfield, and B. Liu, "Theoretical study of the AlO blue-green ($B^2\Sigma^+$ -$X^2\Sigma^+$) band system," *Journal of Quantitative Spectroscopy and Radiative Transfer*, vol. 30, no. 5, pp. 449–462, Nov. 1983.

[9] J. Coxon and S. Naxakis, "Rotational analysis of the $B^2\Sigma^+ - X^2\Sigma^+$ system of the aluminum monoxide radical, AlO," *Journal of Molecular Spectroscopy*, vol. 111, no. 1, pp. 102–113, May 1985.

[10] I. Glassman and R. Yetter, *Combustion*, 4th ed. Elsevier Inc., 2008.

[11] J. Glorian, S. Gallier, and L. Catoire, "On the role of heterogeneous reactions in aluminum combustion," *Combustion and Flame*, 2016.